The Astrophysical Journal, 874:80 (14pp), 2019 March 20 https://doi.org/10.3847/1538-4357/ab0422

High-energy Emission from Interacting Supernovae: New Constraints on Cosmic-Ray Acceleration in Dense Circumstellar Environments

Kohta Murase[1,2,3,4], Anna Franckowiak[5], Keiichi Maeda[6], Raffaella Margutti[7], and John F. Beacom[8,9,10]
[1] Department of Physics, Pennsylvania State University, University Park, PA 16802, USA
[2] Department of Astronomy & Astrophysics, Pennsylvania State University, University Park, PA 16802, USA
[3] Center for Particle and Gravitational Astrophysics, Pennsylvania State University, University Park, PA 16802, USA
[4] Center for Gravitational Physics, Yukawa Institute for Theoretical Physics, Kyoto University, Kyoto, Kyoto 606-8502, Japan
[5] Deutsches Elektronen-Synchrotron (DESY), Platanenallee 6, Zeuthen D-15738, Germany
[6] Department of Astronomy, Kyoto University, Kyoto, Kyoto 606-8502, Japan
[7] Department of Physics and Astronomy, Northwestern University, Evanston, IL 60208, USA
[8] Center for Cosmology and Astro Particle Physics, Ohio State University, Columbus, OH 43210, USA
[9] Department of Physics, Ohio State University, Columbus, OH 43210, USA
[10] Department of Astronomy, Ohio State University, Columbus, OH 43210, USA
Received 2018 July 9; revised 2019 January 18; accepted 2019 February 2; published 2019 March 26

Abstract

Supernovae (SNe) with strong interactions with circumstellar material (CSM) are promising candidate sources of high-energy neutrinos and gamma-rays and have been suggested as an important contributor to Galactic cosmic rays (CRs) beyond 10^{15} eV. Taking into account the shock dissipation by a fast velocity component of SN ejecta, we present comprehensive calculations of the nonthermal emission from SNe powered by shock interactions with a dense wind or CSM. Remarkably, we consider electromagnetic cascades in the radiation zone and subsequent attenuation in the pre-shock CSM. A new time-dependent phenomenological prescription provided by this work enables us to calculate gamma-ray, hard X-ray, radio, and neutrino signals, which originate from CRs accelerated by the diffusive shock acceleration (DSA) mechanism. We apply our results to Type IIn SN 2010jl and Type Ib/IIn SN 2014C, for which the model parameters can be determined from the multiwavelength data. For SN 2010jl, the more promising case, by using the the latest *Fermi* Large Area Telescope Pass 8 data release, we derive new constraints on the CR energy fraction, $\epsilon_p \lesssim 0.05$–0.1. We also find that the late-time radio data of these interacting SNe are consistent with our model. Further multimessenger and multiwavelength observations of nearby interacting SNe should give us new insights into the DSA in dense environments, as well as pre-SN mass-loss mechanisms.

Key words: astroparticle physics – cosmic rays – gamma rays: general – neutrinos – radiation mechanisms: nonthermal – supernovae: general – supernovae: individual (SN 2010jl, SN 2014C)

1. Introduction

Supernovae (SNe) have been widely believed to be the main contributors to Galactic cosmic rays (CRs). The observed CR flux can be explained if $\sim$10% of the SN ejecta energy, $\mathcal{E}_{\rm ej} \sim 10^{51}$ erg, is converted into the kinetic energy of accelerated CR ions. It has been believed that the diffusive shock acceleration (DSA) mechanism is responsible for particle acceleration in supernova remnants (SNRs; see, e.g., Drury 1983, for a review), and SNRs have been observed in gamma-rays with gamma-ray observatories such as *Fermi* and imaging atmospheric Cerenkov telescopes (IACTs) such as H.E.S.S., MAGIC, and VERITAS. Recent detailed observations at sub-GeV energies have led to the discovery of a low-energy cutoff due to neutral pion decay, which is regarded as evidence of hadronic gamma-ray emission from $\pi^0 \to 2\gamma$ (see Funk 2015, and references therein). Independent of these phenomenological and observational arguments, state-of-the-art particle-in-cell simulations have also revealed that CR ions carry $\sim$10% of the SN ejecta energy via the DSA mechanism (e.g., Caprioli 2016).

How early is high-energy nonthermal emission anticipated? Obviously, most of the SN explosion energy remains as bulk kinetic energy until the ejecta begins to decelerate at the Sedov radius. Thus, it has been widely believed that a negligible energy fraction of the SN ejecta energy can be used for high-energy emission in the first several days to months after the explosion. The hydrodynamical evolution of SNe is divided into several phases. Just after the core collapse, an SN shock propagates inside a stellar core or envelope, and the shock is radiation mediated or even collisional (Weaver 1976). As the shock reaches the surface of the progenitor star, the photon diffusion time becomes short enough, and the shock breakout (at which the SN emission begins to escape) occurs (e.g., Matzner & McKee 1999). Then, the SN shock starts to sweep up circumstellar material (CSM),[11] and efficient CR acceleration begins to operate as in SNRs. However, for mass-loss rates that are typical of evolved massive stars, $\sim 10^{-6}$ to $10^{-4}\,M_\odot\,{\rm yr}^{-1}$, high-energy neutrino and gamma-ray emission is detectable only for nearby SN events (Murase 2018), because the SN ejecta are largely in the free expansion phase.

Interestingly, an increasing sample of SNe discovered by recent massive searches for optical and near-IR transients has revealed that strong shock interactions between the SN ejecta and a dense wind or CSM shell occur in various classes of explosive transients, as suggested by observations of Type IIn, Ibn, Ia-CSM, and II superluminous SNe (e.g., Smith et al. 2007; Miller et al. 2009; Ofek et al. 2013a, 2013b, 2014a, 2014b; Margutti et al. 2014a, 2017). This suggests that the pre-explosion eruption of the stellar material or inflation of its envelope might be ubiquitous (see Smith 2014, for a review).

[11] Strictly speaking, the external material can be a dense wind or CSM shell or even an inflated envelope.

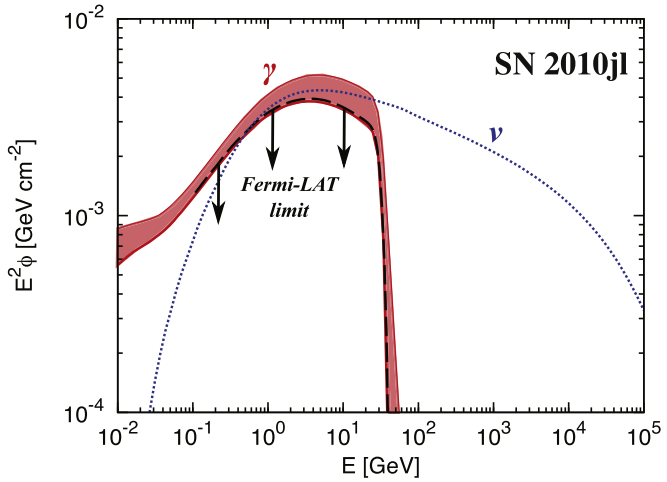

Figure 1. Synthetic spectra for hadronic gamma-ray and all-flavor neutrino spectra from Type IIn SN 2010jl. The CR parameters are $\epsilon_p = 0.05\,(\epsilon_{\rm sn}/0.25)$ and $s_p = 2.2$, and the SN parameters are determined by observations (Ofek et al. 2014b). The upper bound by the 1 yr *Fermi*-LAT observation is indicated by the dashed line with arrows. The upper solid curve of the (red) shaded region indicates the prediction for gamma-rays from the radiation zone, whereas the lower solid curve corresponds to the case where gamma-ray attenuation in the pre-shock CSM is implemented. The dotted curve represents the predicted neutrino spectrum. Note that the fluences integrated from 20 to 316 days are shown. See text for details.

Although the origin of extended material is not well known, significant mass ($\sim 10^{-3}$ to $10\,M_\odot$) may be ejected $\sim$0.1–1 yr before the core-collapse event (e.g., Smith & McCray 2007; Immler et al. 2008; Smith 2013; Fransson et al. 2014; Mauerhan et al. 2014; Milisavljevic et al. 2015). For such objects, the energy dissipated by the shock is significantly enhanced (see review by Chevalier & Fransson 2017), and a substantial amount of CRs will be produced even in the early phase. Murase et al. (2011, 2014) suggested that nonthermal signatures (including neutrinos, gamma-rays, X-rays, submillimeter, and radio waves) can be used as a probe of the early stage of CR acceleration in SNe IIn. The ambient density is so high that most CRs should be converted into neutrino and gamma-ray emission (i.e., the system is "calorimetric"), in which the CR acceleration can be directly tested by high-energy observations via modeling of optical emission from SNe (Margutti et al. 2014a; Ackermann et al. 2015). CR acceleration in dense environments has also been seen by gamma-ray observations of novae (Ackermann et al. 2014). It is worth mentioning that interacting SNe and SNe IIn are much more energetic than novae and have been suggested as PeVatrons, in particular accelerators of CRs beyond the *knee* energy at $10^{15.5}$ eV (Sveshnikova 2003; Murase et al. 2014; Zirakashvili & Ptuskin 2016). They have also been discussed as one of the origins of IceCube's neutrinos above 0.1 PeV (Zirakashvili & Ptuskin 2016; Petropoulou et al. 2017). Thus, searching for high-energy emission will give us clues to the CR origin, as well as mechanisms of early-time particle acceleration and pre-explosion mass losses.

In this work, we present results of detailed calculations of nonthermal emission from interacting SNe. In the early stages of strongly interacting SNe such as SNe IIn, copious thermal photons are present, which inevitably initiate electromagnetic cascades via two-photon annihilation and subsequent synchrotron and inverse Compton radiation. In addition, gamma-rays and radio waves may be attenuated during their propagation in the CSM. The model is described in Section 2, and we apply our phenomenological time-dependent model to SN 2010jl (see Section 3). In particular, using the Pass 8 data of the *Fermi* Large Area Telescope (LAT), we perform detailed analyses of gamma-ray emission from SN 2010jl and compare the limits with predictions of the theoretical model. To convey one of the main results in this work, we first show predicted neutrino and gamma-ray fluences, together with the upper limit by *Fermi*-LAT, in Figure 1. The comparison between the theory and data implies that the energy fraction of CRs is constrained to be $\epsilon_p \lesssim 0.05$–0.1. In Section 4, we provide a simplified time-integrated model, which can be useful when detailed data are not available. The model is then applied to strongly interacting Type Ib SN 2014C, in addition to SN 2010jl. In Section 5, we additionally discuss the gamma-ray detectability of nearby SNe, and the results are summarized in Section 6. We use the notation $Q = 10^x Q_x$ in cgs units unless noted otherwise.

2. High-energy Emission from Interacting Supernovae

2.1. Overview

For a wide range of parameters of SNe indicating interactions with a dense CSM,[12] it has been shown that the SN shock becomes collisionless and non-radiation-mediated when the Thomson optical depth τ_T is less than $\sim c/V_s$ (Katz et al. 2012; Murase et al. 2011). Note that the formation of collisionless shocks around the photon breakout radius $R_{\rm bo}$ would not occur for a steep density profile expected in the outer stellar envelope. The maximum velocity of the pre-shock CSM is limited by the radiation pressure, which implies that the collisionless shock may form at $R_s \gtrsim [2(3-w)/(w-1)]^{1-w} R_{\rm bo}$, where R_s is the shock radius and $w(<3)$ is the ambient density slope.[13] With a CSM (for which $w \sim 0$–2 is typically expected), the shock should become collisionless around $R_{\rm bo}$. Unless the CSM density is too large for Coulomb losses to be relevant (Murase et al. 2014), the CR acceleration will also begin after photons start to escape at the breakout time, $t_{\rm bo}$. Then, CRs interact with CSM nucleons via *pp* interactions, leading to neutrinos, gamma-rays, and X-rays, followed by longer-timescale radio/submillimeter emission from secondary electrons and positrons.

How much is the dissipation energy? In the frequently adopted simplified SN ejecta model, the dissipation energy is estimated to be $M_{\rm cs}\mathcal{E}_{\rm ej}/(M_{\rm ej}+M_{\rm cs})$ (e.g., Murase et al. 2011; Petropoulou et al. 2016), where $M_{\rm cs}$ is the CSM mass and $M_{\rm ej}$ is the ejecta mass. However, the realistic SN ejecta has a density structure as a function of velocity, and there is a high-velocity tail. Murase (2018) considered a time-dependent model, using a self-similar solution (Chevalier 1982; Nadezhin 1985; Moriya et al. 2013). In this more detailed model, as a function of the

[12] We stress that the physical situation is quite different in ordinary SNe such as SNe II-P and II-L, in which the CSM may not be dense enough that we can naturally expect that the conventional DSA operates (Murase 2018). On the other hand, in SNe IIn, the shock is initially radiation mediated, so the onset of CR acceleration is uncertain and worth investigating.

[13] Radiation from downstream can accelerate the CSM up to $\sim K\mathcal{E}_{\rm rad}/(4\pi R_s^2 c)$, where K is the opacity. In the spherical geometry, the radiation energy $\mathcal{E}_{\rm rad}$ is limited by $\sim M_{\rm cs}(<R_s)V_s^2/2$, where $M_{\rm cs}(<R_s) = \int^{R_s} dR\, 4\pi R^2 \varrho_{\rm cs}$. Noting $\varrho_{\rm cs}(R_{\rm bo}) \approx (w-1)c/(KV_sR_{\rm bo})$ from the breakout condition ($\tau_T \sim c/V_s$), we obtain one of the necessary conditions for the onset of collisionless shocks, which implies that CR acceleration occurs for $w \lesssim 3$. Whereas high-energy neutrinos are not promising for breakout emission from the stellar envelope that has a steep density profile, efficient neutrino emission is naturally expected for the breakout from a dense, wind-like or shell-like CSM (Murase 2018).

ejecta velocity (V), the dissipated energy is given by $\mathcal{E}_{\rm ej}(>V) \propto V^{5-\delta}$, where $\mathcal{E}_{\rm ej}(>V) \equiv \int_V dV' (d\mathcal{E}_{\rm ej}/dV')$ and δ is the index of the outer ejecta density profile introduced via $\varrho_{\rm ej} \propto t^{-3}(r/t)^{-\delta}$. Note that $\mathcal{E}_{\rm ej}(>V)$ depends on V, which is different from the "total" ejecta energy $\mathcal{E}_{\rm ej}$. Here one should keep in mind that the higher-velocity ejecta is more efficiently dissipated, which significantly enhances the detectability of high-energy emission compared to the simple estimate (Murase 2018). While $\delta = 10$ (for a convective core with a radiative envelope) and $\delta = 12$ (for a radiative core with a convective envelope) are often assumed (Matzner & McKee 1999), realistic values of δ are uncertain for SNe IIn, because the ejecta may already experience some CSM interactions prior to the major dissipation (van Marle et al. 2010). Note that smaller values of δ are also indicated for trans-relativistic SNe that are associated with low-luminosity GRBs that may be driven by jets (e.g., Margutti et al. 2014b).

We consider an SN shock that propagates in the CSM. For simplicity,[14] we assume a CSM density profile of

$$\varrho_{\rm cs}(R) = \mathcal{D}R^{-w} \equiv DR_0^{-2}\left(\frac{R}{R_0}\right)^{-w}, \quad (1)$$

where $w = 2$ corresponds to the wind density profile. The target nucleon density is given by

$$n_N = \frac{\mathcal{D}}{m_H}R^{-w} \equiv \frac{D}{m_H R_0^2}\left(\frac{R}{R_0}\right)^{-w} \simeq 3.0 \times 10^{10}\,{\rm cm^{-3}}\, D_* R_{0,15}^{w-2} R_{15}^{-w}, \quad (2)$$

where $D_* = D/(5 \times 10^{16}\,{\rm g\,cm^{-1}})$ ($D = \mathcal{D}$ for $w = 2$) and R_0 is an arbitrary radius characterizing the CSM radius. Note that $D_* = 1$ corresponds to $D = \dot{M}_w/(4\pi V_w)$ with a wind mass-loss rate of $\dot{M}_w = 0.1\,M_\odot\,{\rm yr^{-1}}$ and a wind velocity of $V_w = 100\,{\rm km\,s^{-1}}$.

As noted, a faster component of the ejecta is decelerated earlier, and the kinetic luminosity that can be used for dissipation at the forward shock is

$$L_s = \frac{\Delta\Omega}{2}\varrho_{\rm cs}R_s^2 V_s^3 \simeq 3.9 \times 10^{43}\,{\rm erg\,s^{-1}}\, D_* R_{0,15}^{w-2} \times R_{s,15}^{2-w}(V_s/5000\,{\rm km\,s^{-1}})^3, \quad (3)$$

where R_s is the shock radius, V_s is the forward shock velocity, and $\Delta\Omega$ is the effective solid angle of the CSM interaction. In this subsection, $\Delta\Omega = 4\pi$ is used assuming that the CSM is spherical. The bolometric, thermal radiation luminosity (used for thermal SN emission in the optical and/or X-ray bands) is expressed as $L_{\rm rad} = \epsilon_{\rm rad}L_s$, where $\epsilon_{\rm rad}$ is the energy fraction carried by the radiation.

The neutrino and gamma-ray emission is governed by the effective optical depth of inelastic pp interactions, f_{pp}, which is estimated to be

$$f_{pp} \approx \kappa_{pp}\sigma_{pp}cn_N(R_s/V_s) \simeq 27\, D_* R_{0,15}^{w-2} R_{s,15}^{1-w}(V_s/5000\,{\rm km\,s^{-1}})^{-1}, \quad (4)$$

where $\sigma_{pp} \approx 3 \times 10^{-26}\,{\rm cm^2}$ is the inelastic pp cross section and $\kappa_{pp} \approx 0.5$ is the proton inelasticity, respectively. Here we have used $f_{pp} \approx \kappa_{pp}\sigma_{pp}c(r_{\rm sc}n_N)(\Delta_s/V_s) \approx \kappa_{pp}\sigma_{pp}cn_N(R_s/V_s)$, where $r_{\rm sc}$ is the shock compression ratio and $\Delta_s \approx R_s/r_{\rm sc}$ is the size of the shocked region. Because the CR energy density in the post-foward-shock region is estimated to be $\epsilon_p\varrho_{\rm cs}V_s^2/2 = \epsilon_p L_s/(\Delta\Omega R_s^2 V_s)$, for example, the gamma-ray luminosity is given by

$$L_\gamma \approx \frac{1}{3}\min\left[\frac{M_{\rm cs}(<R_s)}{m_H}\kappa_{pp}\sigma_{pp}c\frac{\epsilon_p L_s}{\Delta\Omega R_s^2 V_s},\ \epsilon_p L_s\right] \approx \frac{1}{3}\min[f_{pp},\,1]\,\epsilon_p L_s, \quad (5)$$

where ϵ_p is the energy fraction of accelerated CR protons and $\sim$0.1 is typically expected in the DSA theory for quasi-parallel shocks (Caprioli & Spitkovsky 2014a). Such a value is also motivated by the hypothesis that interacting SNe are responsible for the observed CR flux around or beyond the knee energy at $\sim$3 PeV (Sveshnikova 2003; Murase et al. 2014). The factor $1/3$ comes from π^+: π^-: $\pi^0 \approx$1:1:1 in high-energy inelastic pp interactions. Note that $M_{\rm cs}(<R_s) = \Delta\Omega D R_s$ in the wind case.

The principal parameters are CSM nucleon density n_N, shock radius R_s, and shock velocity V_s (Murase et al. 2011; Margutti et al. 2014a). The differential gamma-ray luminosity is approximately

$$E_\gamma L_{E_\gamma} \equiv E_\gamma\frac{dL_\gamma}{dE_\gamma} \approx \frac{1}{3}\min[f_{pp},\,1]E_pL_{E_p} \simeq 1.3 \times 10^{41}\ {\rm erg\,s^{-1}}\ \min[f_{pp},\,1] \times \left(\frac{E_\gamma}{0.1m_pc^2}\right)^{2-s_p}\epsilon_{p,-1}\mathcal{R}_{p0,1}^{-1} \times D_* R_{0,15}^{w-2}R_{s,15}^{2-w}(V_s/5000\,{\rm km\,s^{-1}})^3, \quad (6)$$

where s_p is the proton spectral index and $\mathcal{R}_{p0} \sim$ 5–10 is the normalization factor that is given by

$$E_pL_{E_p} \equiv E_p\frac{dL_p}{dE_p} = \frac{\epsilon_pL_s}{\mathcal{R}_{p0}}\left(\frac{E_p}{m_pc^2}\right)^{2-s_p}. \quad (7)$$

Here E_p is the CR proton energy and $E_pL_{E_p}$ is the CR luminosity per logarithmic energy.

In DSA, CRs are accelerated via scatterings with plasma or magnetohydrodynamic waves, and efficient amplification of the magnetic field in both the upstream and downstream regions is naturally expected for SN shocks. We parameterize the magnetic field by $U_B \equiv \epsilon_B(\varrho_{\rm cs}V_s^2/2)$ (where U_B is the magnetic energy density), which leads to

$$B = (\epsilon_B 4\pi\varrho_{\rm cs}V_s^2)^{1/2} \simeq 40\ {\rm G}\ \epsilon_{B,-2}^{1/2}D_*^{1/2}R_{0,15}^{w/2-1}R_{s,15}^{-w/2}(V_s/5000\,{\rm km\,s^{-1}}), \quad (8)$$

where $\epsilon_B \sim$ 0.001–0.01 is assumed. Although such a value is motivated by observations of radio SNe (e.g., Chevalier et al. 2006; Maeda 2012) and the hypothesis that these SNe contribute to the observed CR flux beyond the knee energy, it is highly uncertain whether the maximum CR energy can exceed $\sim$10–100 TeV. Indeed, the significant amplification of

[14] The CSM profile may not be a simple power law, and the shell-like structure has often been observed (e.g., Margutti et al. 2017). In general, we may not apply self-similar solutions to describe the shock dynamics.

magnetic fields may occur by various physical reasons. The CSM could be highly turbulent and magnetized, because the violent CSM eruptions may also be accompanied by shocks (Murase et al. 2014). The CSM may also be highly clumpy (Smith et al. 2009), in which case the turbulent dynamo process could amplify both upstream and downstream fields (e.g., Xu & Lazarian 2017). The upstream magnetic field amplification with $\epsilon_B \propto \epsilon_p \mathcal{M}_A^{-1}$ (where $\mathcal{M}_A$ is the Alfvénic Mach number) could also be realized by CRs themselves via streaming instabilities (Caprioli & Spitkovsky 2014b). The CR spectrum can also be affected by neutral particles (Murase et al. 2011), and the maximum energy can be limited by the ionized region as an escape boundary (whose size is $\sim 0.5 \times 10^{15}\,{\rm cm}\,(1+\tau_T)^{-1/3} L_{X,43}^{1/3} \nu_{18}^{-1/3} n_{N,10}^{-2/3} (\mathcal{T}^u_{\rm cs,5})^{1/4}$ for the intrinsic X-ray luminosity L_X and the pre-shock CSM temperature $\mathcal{T}^u_{\rm cs}$). We simply determine the maximum CR energy by comparing the acceleration time with the dynamical time and energy-loss time. This should be sufficient because our results on GeV–TeV emission are largely insensitive to the maximum energy.

Secondary electrons and positrons lose their energies via synchrotron cooling, and their characteristic frequency is

$$\nu_h \sim \frac{3}{4\pi}\left(\frac{m_\pi}{4m_e}\right)^2 \frac{eB}{m_e c} \simeq 780\ {\rm GHz}\ \epsilon_{B,-2}^{1/2} D_*^{1/2} R_{0,15}^{w/2-1} \times R_{s,15}^{-w/2} (V_s/5000\ {\rm km\ s^{-1}}). \quad (9)$$

Assuming the fast cooling (i.e., electrons at the injection frequency cool within the dynamical time), the resulting synchrotron luminosity from CR-induced electrons and positrons (at $\nu < \nu_h$) is

$$\begin{aligned} \nu L_\nu^h &\approx \frac{1}{2(1+Y)} \frac{1}{6} \min[f_{pp}, 1] E_p L_{E_p} \\ &\simeq 3.3 \times 10^{40}\ {\rm erg\ s^{-1}}\ \min[f_{pp}, 1](1+Y)^{-1} \\ &\quad \times \left(\frac{\nu}{\nu_h}\right)^{1/2} \epsilon_{p,-1} \mathcal{R}_{p0,1}^{-1} \\ &\quad \times D_* R_{0,15}^{w-2} R_{s,15}^{2-w} (V_s/5000\ {\rm km\ s^{-1}})^3 f_{\rm esc}, \end{aligned} \quad (10)$$

where Y is the inverse Compton Y parameter and $f_{\rm esc}$ is the escape fraction of radio waves. The escape fraction is phenomenologically introduced to represent effects of various low-energy photon absorption processes (Murase et al. 2014).

Follow-up observations at high-frequency radio bands are important (Murase et al. 2014; Petropoulou et al. 2016), and the hadronic scenario predicts

$$\begin{aligned} \frac{E_\gamma F_{E_\gamma}}{\nu F_\nu^h} &\approx 4 \left(\frac{E_\gamma}{0.1 m_p c^2}\right)^{2-s_p} \left(\frac{\nu}{\nu_h}\right)^{1/2} \\ &\sim 0.9 \left(\frac{E_\gamma}{1\ {\rm GeV}}\right)^{2-s_p} \left(\frac{\nu}{100\ {\rm GHz}}\right)^{1/2} \epsilon_{B,-2}^{-1/4} D_*^{-1/4} \\ &\quad \times R_{0,15}^{1/2-w/4} R_{s,15}^{w/4} (V_s/5000\ {\rm km\ s^{-1}})^{-1/2} f_{\rm esc}^{-1}, \end{aligned} \quad (11)$$

where $E_\gamma F_{E_\gamma}$ and νF_ν^h are gamma-ray and radio energy fluxes observed at Earth, respectively. Here the numerical value in the last expression is evaluated for $s_p = 2.2$ and $Y \ll 1$ is assumed. As long as $s_p \sim 2$, the ratio of the gamma-ray to submillimeter energy fluxes is expected to be a weak function of time and is predicted to be of the order of unity for SNe IIn with $D_* \sim 0.1$–10. The CR index at sufficiently high energies could be modified in radiative shocks, because a higher compression ratio (i.e., $r_s \gg 4$) could make the spectrum harder (e.g., Yamazaki et al. 2006).

As commonly expected in ordinary radio SNe, primary electrons will also be accelerated. The observed CR proton and electron fluxes on Earth and the measurements of Galactic SNRs suggest that the ratio of electron to proton fluxes at the same energy is $\sim 10^{-3}$ to 10^{-2}, implying that the energy fraction carried by DSA-accelerated CR electrons is $\epsilon_e \sim 10^{-4}$ to 10^{-3} for a flat energy spectrum (e.g., Katz & Waxman 2008). Electrons can be injected into the DSA once their Lorentz factor exceeds the shock transition layer, and we assume that the corresponding characteristic Lorentz factor is given by $\gamma_{l2} \sim (m_p/m_e)(V_s/c)$, above which the spectral index is $s_e = s_p$ (e.g., Park et al. 2015). For $\gamma_{l2} \gg 1$, the characteristic synchrotron frequency for the DSA is estimated to be

$$\nu_{l2} = \frac{3}{4\pi} \gamma_{l2}^2 \frac{eB}{m_e c} \sim 160\ {\rm GHz}\ \epsilon_{B,-2}^{1/2} D_*^{1/2} R_{0,15}^{w/2-1} \times R_{s,15}^{-w/2} (V_s/5000\ {\rm km\ s^{-1}})^3. \quad (12)$$

Note that the conventional DSA may not be applied for electrons with lower Lorentz factors. It has been suggested that observations of SNe IIb and SNe IIn will enable us to probe electron acceleration in the shock transition layer (Maeda 2012, 2013; Murase et al. 2014). For a low-energy component of nonthermal electrons, the injection Lorentz factor is given by $\gamma_{l1} = [1 + (p_{l1}/m_e c)^2]^{1/2}$, where p_{l1} is the corresponding injection momentum. If $p_{l1} \gg m_e c$, we have the conventional formula $\gamma_{l1} = [(g_e \tilde{\epsilon}_e m_p)/(2 f_e m_e)](V_s/c)^2$, where $\tilde{\epsilon}_e$ is the energy fraction of electrons with $\gamma_e \geqslant \gamma_{l1}$, f_e is the number fraction, and $g_e = (q_e - 2)/(q_e - 1)$ for a low-energy spectral index, $q_e > 2$. We typically expect $p_{l1} \lesssim m_e c$, where one may approximate a low-energy electron spectrum as $dn_{{\rm CR}e}/d\gamma_e \propto \gamma_e^{-q_e}$ with $\gamma_{l1} = 1$. The steady-state index of electrons can be ~ 3 owing to radiative energy losses, in which $q_e \sim s_e$ is possible (Chevalier et al. 2006). Or, perhaps, $q_e > s_e$ (allowing $\tilde{\epsilon}_e \sim 0.01$) could be realized by other processes such as the shock-drift acceleration mechanism at quasi-perpendicular shocks (e.g., Matsumoto et al. 2017).

The high-frequency synchrotron luminosity (at $\nu > \nu_{l2}$) in the fast-cooling case is

$$\begin{aligned} \nu L_\nu^{l2} &\approx \frac{1}{2(1+Y)} E_e L_{E_e} \\ &\simeq 2.0 \times 10^{38}\ {\rm erg\ s^{-1}}\ (1+Y)^{-1} \left(\frac{\nu}{\nu_{l2}}\right)^{\frac{2-s_e}{2}} \epsilon_{e,-4} \mathcal{R}_{e0,1}^{-1} \\ &\quad \times D_* R_{0,15}^{w-2} R_{s,15}^{2-w} (V_s/5000\ {\rm km\ s^{-1}})^3 f_{\rm esc}, \end{aligned} \quad (13)$$

where $\epsilon_e(<\tilde{\epsilon}_e)$ is the energy fraction of DSA-accelerated electrons. Thus, the leptonic origin of radio emission predicts

$$\frac{E_\gamma F_{E_\gamma}}{\nu F_\nu^{l2}} \approx \frac{2\epsilon_p}{3\epsilon_e}\frac{\mathcal{R}_{e0}}{\mathcal{R}_{p0}}\left(\frac{E_\gamma}{0.1 m_p c^2}\right)^{2-s_p}\left(\frac{\nu}{\nu_{l2}}\right)^{\frac{s_e-2}{2}} \min[f_{pp},\,1]$$
$$\sim 400\,\left(\frac{E_\gamma}{1\ \mathrm{GeV}}\right)^{2-s_p}\left(\frac{\nu}{100\ \mathrm{GHz}}\right)^{\frac{s_e-2}{2}}(10^{-3}\epsilon_p/\epsilon_e)$$
$$\times\,(\mathcal{R}_{e0}/\mathcal{R}_{p0})\,\epsilon_{B,-2}^{\frac{2-s_e}{4}} D_*^{\frac{2-s_e}{4}} R_{0,15}^{\frac{(w-2)(2-s_e)}{4}} R_{s,15}^{\frac{w(s_e-2)}{4}}$$
$$\times\,(V_s/5000\ \mathrm{km\ s^{-1}})^{\frac{3(2-s_e)}{2}} \min[f_{pp},\,1] f_{\rm esc}^{-1}, \quad (14)$$

where $Y \ll 1$ is assumed. The ratio depends on R_s and V_s differently from that in the hadronic scenario, so the time dependence of the gamma-ray to radio fluxes is relevant to discriminate between the hadronic and leptonic interpretations. So far, we have ignored various processes that can suppress the radio emission. More generally, low-frequency emission is affected by various effects such as synchrotron self-absorption, free–free absorption, and Coulomb cooling, which will be included in our numerical calculations.

In SNe IIn, $\epsilon_p \gg \epsilon_e$ allows us to expect that both gamma-ray emission and high-frequency radio emission are dominated by the hadronic component. In the high-frequency limit (i.e., $\nu > \nu_h, \nu_{l2}$), in which either the hadronic or leptonic scenario predicts the same spectrum, $\nu F_\nu \propto \nu^{2-\beta}$ (where β is the photon index), the condition for the secondary emission to overwhelm the primary component is written as

$$\min[1, f_{pp}]\frac{\epsilon_{p,-1}}{\epsilon_{e,-4}}\left(\frac{\nu_{l2}}{\nu_h}\right)^{2-\beta} \gtrsim 6\times 10^{-3}, \quad (15)$$

where $\mathcal{R}_{p0} = \mathcal{R}_{e0}$ and $s = s_p = s_e$ are assumed and $\beta = 1 + s/2$ is the high-energy synchrotron photon index predicted by theory.[15] Here s is the spectral index of CR protons and electrons that are accelerated by DSA.

In astrophysical environments, high-energy neutrinos should be produced by hadronic processes like the *pp* reaction, so they serve as a unique, powerful probe of CR ion acceleration. On the other hand, electromagnetic emissions originate from both hadronic and leptonic processes. In the hadronic scenario, gamma-rays are mainly produced by neutral pions and cascades from secondary electrons and positrons, while radio emission is attributed to synchrotron radiation from the secondaries. In the leptonic scenario, gamma-rays mainly originate from inverse Compton radiation by primary electrons, while radiation emission is ascribed to synchrotron radiation from the same primary electrons. In realistic situations, we should expect both components, but the hadronic component is likely to be dominant when DSA occurs in dense environments (Murase et al. 2014).

2.2. Phenomenological Model

In cases of well-observed SNe IIn such as SN 2010jl, parameters on SN dynamics can be determined by the observational data of (mostly) thermal emission from the SNe. We here focus on the forward shock emission (see Murase et al. 2011; Chevalier & Fransson 2017, for a discussion on the reverse shock emissions) and consider a single radiation zone with the size $\Delta R_s \approx R_s$. In a time-dependent model, we need to know three quantities, $\varrho_{\rm cs}$, R_s, and V_s as a function of time t. If all three quantities are described by power laws, which are assumed throughout this work for simplicity, one needs five parameters, D, w, R_0, t_0, and the temporal index a, to describe the SN dynamics. Here, just for convenience, we take $R_0 = R_{\rm bo}$ and $t_0 = t_{\rm bo}$, where $R_{\rm bo}$ is the photon breakout radius and $t_{\rm bo}$ is the breakout time. Our formalism enables us to predict nonthermal fluxes from the observational data only with a few free parameters such as ϵ_p and s_p. Note that the calculation frameworks used in Murase (2018) and this work are applicable to any type of SNe that cause interactions with the CSM. For example, not only Type IIn and Type Ibn can be the sources of high-energy neutrinos and gamma-rays. High-energy emissions from CSM interactions for Type II-P, II-L, and IIb SNe were first studied by Murase (2018). SNe IIn (whose optical emission is powered by the CSM interactions) are typically expected to have the most powerful nonthermal emissions among these SN classes, and extragalactic objects are detectable (see Section 5 for details). The CSM mass indicated for SNe IIn can be as large as $M_{\rm cs} \sim$ (1–10) $M_{\rm cs}$.

The CSM density given by Equation (1) can be rewritten as

$$\varrho_{\rm cs}(R) = D R_{\rm bo}^{-2}\left(\frac{R}{R_{\rm bo}}\right)^{-w}, \quad (16)$$

where $R_0 = R_{\rm bo}$ is used. The CSM nucleon density is given by $n_N = \varrho_{\rm cs}/m_H$.

Assuming a power-law evolution, the shock radius and velocity are parameterized as

$$R_s = R_{\rm bo}\left(\frac{t}{t_{\rm bo}}\right)^a \quad (17)$$

and

$$V_s = V_{\rm bo}\left(\frac{t}{t_{\rm bo}}\right)^{a-1}, \quad (18)$$

where $V_{\rm bo} = aR_{\rm bo}/t_{\rm bo}$. Note that R_s and V_s are determined by the observational data. If the self-similar solution for a spherical CSM is adopted, the index a is explicitly given by $a = (\delta - 3)/(\delta - w)$, where $\delta \sim 7$–12 is the index of the outer ejecta profile, $\varrho_{\rm ej} \propto t^{-3}(r/t)^{-\delta}$ (e.g., Matzner & McKee 1999).

The shock power is calculated as

$$L_s = \left(\frac{\Delta\Omega}{2}\right) D V_{\rm bo}^3\left(\frac{t}{t_{\rm bo}}\right)^{5a-3-aw} \propto t^{-\alpha}, \quad (19)$$

where $\alpha = 3 - a(5 - w)$. If we assume the self-similar solution, which is valid until the deceleration of the inner ejecta starts, we obtain $\alpha = [(\delta - 3)(w - 2) + 3(3 - w)]/(\delta - w)$ (e.g., Moriya et al. 2013; Ofek et al. 2014b; Chevalier & Fransson 2017; Murase 2018). Note that $\Delta\Omega = 4\pi$ in the spherical geometry of the CSM, and it has been argued that the CSM could be aspherical or even clumpy (e.g., Smith et al. 2009; Margutti et al. 2014a; Smith 2014; Katsuda et al. 2016). Only a fraction ($\epsilon_{\rm rad} < 1$)

[15] We note that Murase et al. (2014) used $\epsilon_e = 10^{-4}$ in Equations (58) and (59) and q should be the photon index there.

of the shock power is used for the radiation luminosity, $L_{\rm rad} = \epsilon_{\rm rad} L_s$.

We assume that the DSA works as in SNRs and consider a power-law form,

$$\frac{dn_{{\rm CR}p}}{dp} \propto p^{-s_p} e^{-p/p_{\rm max}}, \tag{20}$$

where $n_{{\rm CR}p}$ is the CR proton number density and $dn_{{\rm CR}p}/dp$ is the differential momentum distribution. The maximum momentum, $p_{\rm max}$, is determined by CR escape and cooling processes such as pp interactions, Bethe–Heitler pair production, and adiabatic losses.[16] We also introduce an escape boundary of $0.6R_s$ to estimate the maximum energy. The escape boundary is assumed to be $\sim(0.1$–$1)R_s$ for SNRs to explain the observed CR flux (Ohira et al. 2010), and our results are insensitive to its exact value. The DSA thoery for a quasi-parallel shock predicts $s_p = 2.0$, whereas a steeper spectrum of $s_p \sim 2.2$–2.4 is inferred by GeV–TeV gamma-ray observations of the young SNR Cas A (e.g., Ahnen et al. 2018, and references therein).

The normalization of the CR spectrum is given by

$$U_p = \int^{p_{\rm max}} dp\, E_p \frac{dn_{{\rm CR}p}}{dp}, \tag{21}$$

where the CR proton energy density $U_p \approx \epsilon_p L_s/(\Delta\Omega R_s^2 V_s)$ is used. Throughout this work, we choose $\epsilon_p = 0.05$ as a fiducial parameter, based on the observation of Cas A (Ahnen et al. 2018). We only consider fresh CRs because the CRs lose their energies via adiabatic losses during the dynamical time (as well as via other energy-loss processes). A more quantitative treatment is possible by solving kinetic equations of protons, which is important only if the luminosity declines more rapidly than $L_s \propto t^{-1}$. Our assumption to consider the fresh CRs is justified for $w < 3$ and indeed seen in intensively studied SNe IIn (Moriya et al. 2013). Such an approximation is often used in the context of GRBs (Mészáros 2006; Murase 2008). Importantly, when the hadronic cooling of CR protons is dominant and its effective timescale, $t_{pp} \approx (\kappa_{pp}\sigma_{pp} n_N c)^{-1}$, is shorter than the dynamical time, $t_{\rm dyn} \approx R_s/V_s$, the luminosity of secondary particles such as neutrinos and gamma-rays is limited by L_p (see Equation (5)). The system is "calorimetric," and energy conservation should not be violated.

For a given set of parameters describing hydrodynamics evolution of the parameters, we calculate energy densities of neutrinos, gamma-rays, and electrons/positrons, by exploiting the following formulae:

$$\begin{aligned}
\dot{n}^{\rm inj}_{E_\nu} &= \frac{d\sigma_{pp}\xi_\nu}{dE_\nu}\frac{cM_{\rm cs}}{m_H \mathcal{V}}\int^{p_{\rm max}} dp\, E_p \frac{dn_{{\rm CR}p}}{dp} \\
\dot{n}^{\rm inj}_{E_\gamma} &= \frac{d\sigma_{pp}\xi_\gamma}{dE_\gamma}\frac{cM_{\rm cs}}{m_H \mathcal{V}}\int^{p_{\rm max}} dp\, E_p \frac{dn_{{\rm CR}p}}{dp} \\
\dot{n}^{\rm inj}_{E_e} &= \frac{d\sigma_{pp}\xi_e}{dE_e}\frac{cM_{\rm cs}}{m_H \mathcal{V}}\int^{p_{\rm max}} dp\, E_p \frac{dn_{{\rm CR}p}}{dp},
\end{aligned} \tag{22}$$

where ξ_ν, ξ_ν, and ξ_e represent multiplicities of the secondaries. We use the differential cross sections of pp interactions given by Kelner et al. (2006), and the total pp cross section is adjusted to the post-Large-Hadron-Collider formula by Kafexhiu et al. (2014). Here the volume of the radiation zone is approximated as $\mathcal{V} \approx \Delta\Omega R_s^3/3$.

In the previous work, Murase et al. (2011), the secondary emissions were calculated ignoring effects of electromagnetic cascades. In this work, using the code that was previously developed in Murase (2018), we solve the following kinetic equations:

$$\begin{aligned}
\frac{\partial n^e_{E_e}}{\partial t} &= \frac{\partial n^{(\gamma\gamma)}_{E_e}}{\partial t} - \frac{\partial}{\partial E_e}[(P_{\rm IC} + P_{\rm syn} + P_{\rm ff} + P_{\rm ad} + P_{\rm Cou}) n^e_{E_e}] \\
&\quad + \dot{n}^{\rm inj}_{E_e}, \\
\frac{\partial n^\gamma_{E_\gamma}}{\partial t} &= -\frac{n^\gamma_{E_\gamma}}{t_{\gamma\gamma}} - \frac{n^\gamma_{E_\gamma}}{t_{\rm mat}} - \frac{n^\gamma_{E_\gamma}}{t_{\rm esc}} + \frac{\partial n^{\rm (IC)}_{E_\gamma}}{\partial t} + \frac{\partial n^{\rm (syn)}_{E_\gamma}}{\partial t} \\
&\quad + \frac{\partial n^{\rm (ff)}_{E_\gamma}}{\partial t} + \dot{n}^{\rm inj}_{E_\gamma},
\end{aligned} \tag{23}$$

where

$$\begin{aligned}
t^{-1}_{\gamma\gamma} &= \int dE_\gamma\, n^\gamma_{E_\gamma} \int \frac{d\cos\theta}{2}\, \tilde{c}\sigma_{\gamma\gamma}, \\
\frac{\partial n^{\rm (IC)}_{E_\gamma}}{\partial t} &= \int dE_e\, n^e_{E_e} \int dE_\gamma\, n^\gamma_{E_\gamma} \int \frac{d\cos\theta}{2}\, \tilde{c}\frac{d\sigma_{\rm IC}}{dE_\gamma}, \\
\frac{\partial n^{(\gamma\gamma)}_{E_e}}{\partial t} &= \frac{1}{2}\int dE_\gamma\, n^\gamma_{E_\gamma} \int dE'_\gamma\, n^\gamma_{E'_\gamma} \int \frac{d\cos\theta}{2}\, \tilde{c}\frac{d\sigma_{\gamma\gamma}}{dE_e},
\end{aligned}$$

and $\partial n^{\rm (ff)}_{E_\gamma}/\partial t$ represents bremsstrahlung emission from nonthermal electrons and positrons (Jackson 1975). Here $\tilde{c} = (1 - \cos\theta)c$ (where θ is the angle between two particles), $t_{\gamma\gamma}$ is the two-photon annihilation time, $t_{\rm mat}$ is the energy-loss time due to Compton scattering and Bethe–Heitler pair-production (Chodorowski et al. 1992) processes, $t_{\rm esc} \approx R_s/c$ is the photon escape time, $P_{\rm IC}$ is the inverse Compton energy-loss rate (where the Klein–Nishina effect is fully taken into account), $P_{\rm syn}$ is the synchrotron energy-loss rate (Rybicki & Lightman 1979), $P_{\rm ff}$ is the nonthermal bremsstrahlung energy-loss rate (Schlickeiser 2002), $P_{\rm ad}$ is the adiabatic energy-loss rate, and $P_{\rm Cou}$ is the Coulomb energy-loss rate (Schlickeiser 2002). The calculation during $t_{\rm dyn} \approx R_s/V_s$ essentially leads to quasi-steady photon spectra at t.

We parameterize the magnetic field in the radiation zone by $\epsilon_B \sim 10^{-3}$ to 10^{-1} against the ram pressure.[17] Note that predictions for high-energy neutrinos depend only on ϵ_p, s_p, and ϵ_B, when all parameters on the SN dynamics are determined by the observational data.

On the other hand, electromagnetic spectra are largely affected by the SN thermal radiation itself and various attenuation processes in the CSM. First, assuming a graybody

[16] At sufficiently high energies, the wave damping due to neutral–ion collisions in the upstream region can be relevant as in partially ionized shocks of SNRs (Murase et al. 2011), but GeV–TeV gamma-ray and neutrino emission would not be much affected.

[17] Alternatively, one can introduce the magnetic field as $U_B \equiv \varepsilon_B \mathcal{E}_s/\mathcal{V}$, where $\mathcal{E}_s \approx L_s(R_s/V_s)$ is the dissipation energy.

spectrum, we introduce the SN optical emission as

$$L_{\rm sn} = L_{\rm sn\,0}\left(\frac{t}{t_{\rm bo}}\right)^{-b_1} \tag{24}$$

for the optical luminosity and

$$\mathcal{T}_{\rm sn} = \mathcal{T}_{\rm sn\,0}\left(\frac{t}{t_{\rm bo}}\right)^{-b_2} \tag{25}$$

for the temperature. The thermal energy may be efficiently converted into radiation via bremsstrahlung or Compton scattering. If the thermalization efficiently proceeds, a significant fraction of the radiation luminosity is released as the SN emission in the optical band. Then, we expect $L_{\rm rad} \approx L_{\rm sn} = \epsilon_{\rm sn} L_s$ with $b_1 = \alpha$. Note that the shock power is estimated from the optical luminosity by $L_s = L_{\rm sn}/\epsilon_{\rm sn}$. In the SN 2010jl case we discuss below, we also use a graybody spectrum and adopt $b_2 = 0$ for simplicity. The SN thermal radiation energy density at R_s is

$$U_{\rm sn} \approx \frac{(1+\tau_T) 3 L_{\rm sn}}{4\pi R_s^2 c}. \tag{26}$$

When the two-photon annihilation optical depth in the radiation zone, $\tau_{\gamma\gamma}$, is larger than unity, this external radiation field unavoidably develops an electromagnetic cascade, which can also suppress the gamma-ray spectrum in the TeV range as we see below. In addition, we include the X-ray emission originating from thermal bremsstrahlung. The total radiation luminosity from thermal particles is $L_{\rm rad} \approx L_{\rm sn} + L_X$. We use $L_X \approx \min[L_{\rm ff}, 0.5 L_s]$, where $L_{\rm ff}$ is the luminosity of thermal bremsstrahlung emission (e.g., Rybicki & Lightman 1979; Murase et al. 2014). The immediate post-shock temperature is determined by the shock velocity V_s, which typically lies in the X-ray range (e.g., Chevalier & Fransson 2017). Note that the observed X-ray luminosity is generally much lower than L_X for the radiation zone, due to the photoelectric absorption in the pre-shock CSM (e.g., Chevalier & Fransson 2017). Considering the thermalization, the average X-ray energy density is estimated to be $U_X \approx 3 L_X/(4\pi R_s^2 c)/(1+\tau_T)$. However, the inclusion of X-rays does not essentially affect the results on nonthermal spectra.

Next, we consider absorption processes for photons escaping from the radiation zone. The screen region is essentially the far upstream of the forward shock. Gamma-rays are further attenuated via the two-photon annihilation process by the SN photons scattered in the pre-shock CSM, as well as via Compton scattering, Bethe–Heitler pair production, and photoelectric absorption by interactions with the matter. Denoting energy-dependent optical depths to each process by $\tau^u_{\gamma\gamma}$, $\tau^u_{\rm Comp}$, $\tau^u_{\rm BH}$, and $\tau^u_{\rm pe}$, we phenomenologically implement the suppression factor, $f_{\rm sup} = \exp(-\tau^u_{\gamma\gamma}) f^{\rm mat}_{\rm sup}$, where $f^{\rm mat}_{\rm sup} = \exp(-\kappa_{\rm Comp}\tau^u_{\rm Comp} - \kappa_{\rm BH}\tau^u_{\rm BH} - \tau^u_{\rm pe})$, with $\kappa_{\rm Comp}$ and $\kappa_{\rm BH}$ being energy-dependent inelasticities (Murase et al. 2015). A fraction of the SN photons scattered at R is $\sim\tau_T(R)$, and the radiation field drops with the inverse-square law. Ignoring details of the geometrical effect for simplicity, we approximately use $\tau^u_{\gamma\gamma} \approx \tau_T \tau_{\gamma\gamma}(1+\tau_T)^{-1} w^{-1}$. The cross section of the Bethe–Heitler process depends on the nucleus charge. Throughout this work, we assume a mass composition of $x_{\rm H} = 0.7$, $x_{\rm He} = 0.25$, and $x_{\rm C/O} = 0.05$, leading to the effective charge, $\tilde{Z}_{\rm eff} \equiv \Sigma_i (2Z_i^2/A_i) x_i = 2.25$, and the inverse of the mean molecular weight per electron, $\mu_e^{-1} = 0.85$. At lower energies, the photoionization and excitation become relevant, for which we adopt the simple approximate opacity, $K_{\rm pe} \simeq 2.4 \times 10^{-2}\,{\rm cm^2\,g^{-1}}\,(h\nu/10\,{\rm keV})^{-3}$ (Morrison & McCammon 1983). For SNe IIn, nonthermal X-ray emission is usually masked by the thermal bremsstrahlung component, and our work has a greater focus on gamma-rays and radio waves.

On the other hand, radio emission is affected by the synchrotron self-absorption, free–free absorption by free electrons, and the so-called Razin–Tsytovich effect. We implement $[1-\exp(-\tau_{\rm sa})]/\tau_{\rm sa}$ for the self-absorption in the radiation zone, where $\tau_{\rm sa}$ is calculated for the energy distribution of electrons and positrons, obtained by our numerical calculations (Rybicki & Lightman 1979). The free–free absorption optical depth, $\tau^u_{\rm ff}$, is

$$\tau_{\rm ff}(\nu) \approx \int_{R_s} dR\; 8.5 \times 10^{-28} \left(\frac{\nu}{10^{10}\,{\rm Hz}}\right)^{-2.1} n_e^2 \times \left(\frac{\mathcal{T}^u_{\rm cs}}{10^4\,{\rm K}}\right)^{-1.35} \left(\frac{1-{\rm e}^{-h\nu/k\mathcal{T}^u_{\rm cs}}}{h\nu/k\mathcal{T}^u_{\rm cs}}\right), \tag{27}$$

ignoring the detailed dependence on the metallicity. We expect that the immediate upstream region is ionized by X-rays, and we use $f^{\rm mat}_{\rm sup} = \exp(-\tau^u_{\rm ff})$. Note that $\mathcal{T}^u_{\rm cs}$ is a pre-shock CSM temperature. Because the far-upstream region is expected to be partially ionized or nearly neutral, the above estimate gives conservative results. We also include the Razin–Tsytovich effect simply by $f^{\rm mat}_{\rm sup} = \exp(-\nu_{\rm RT}/\nu)$, where $\nu_{\rm RT}$ is the Razin–Tsytovich frequency. See discussions in Murase et al. (2014) for details of these physical effects.

The differential luminosity of nonthermal radiation is calculated by

$$E_\gamma L_{E_\gamma} = \frac{(E_\gamma^2 n_{E_\gamma}) \mathcal{V} f_{\rm sup}}{t_{\rm esc}}. \tag{28}$$

For a clumpy or aspherical CSM, the attenuation due to matter (not radiation) can be significantly alleviated, which is especially important for the detectability of radio emission. In such a case, one could replace the suppression factor due to interactions with matter ($f^{\rm mat}_{\rm sup}$) with $\max[f^{\rm mat}_{\rm sup}, f^{\rm mat}_{\rm esc}]$, where $f^{\rm mat}_{\rm esc}$ is the photon escape fraction that depends on details of the CSM geometry. Note that $f_{\rm sup} = 1$ for neutrinos, and the flavor mixing is taken into account.

3. Application to SN 2010jl

3.1. Theoretical Prediction

We apply our calculation method to SN 2010jl, adopting the physical parameters estimated by Ofek et al. (2014b) (see Table 1). SN 2010jl was found in the star-forming galaxy UGC 5189A, whose redshift is $z = 0.0107$, corresponding to a distance of $d = 49$ Mpc (Ofek et al. 2014b). The SN coordinates are R.A. $= 09^{\rm h}42^{\rm m}53\overset{\rm s}{.}3$ and decl. $= +09°29'42''$.

Although our results on gamma-rays are unaffected by interactions with X-rays, we also include thermal X-rays as an additional photon field. For simplicity, the X-ray energy density at the source is implemented by using the formula of bremsstrahlung emission with an immediate downstream temperature of $(3/16)\mu m_H V_s^2$, where μ is the mean molecular weight. (Note that the post-shock temperature can be much

Table 1
Source Parameters of SN 2010jl, Used in Our Time-dependent Model

D_*	w	$t_{\rm bo}$ (days)	$R_{\rm bo}$ (cm)	a	$L_{\rm sn0}$ (erg s^{-1})	$\mathcal{T}_{\rm sn\,0}$ (K)	ϵ_B	ϵ_p
6	2	20	1.1×10^{15}	0.875	5.5×10^{43}	9000	1.5×10^{-2}	0.05

Note. See text for details (see also Ofek et al. 2014b). The derived shock power corresponds to $\epsilon_{\rm sn} = 0.25$.

lower in the far downstream for a radiation-dominated or radiative shock.)

The results on modeled gamma-ray spectra and light curves are shown in Figures 2 and 3. We consider hadronic gamma-ray production, and one sees that pionic gamma-rays give a dominant contribution. Gamma-ray attenuation by the Bethe–Heitler pair-production process in the CSM is important at early times around the photon breakout time, but at late times the gamma-ray flux is only moderately suppressed below ∼20–30 GeV. Note that this effect is less important if the shock velocity is higher (Murase et al. 2014), and its overall influence on the fluence (to $t \sim 300$ days) is only a factor of 2 at most (see Figure 1). This means that GeV gamma-rays can be used as a much more direct probe of shock interactions in dense environments such that $\tau_T > 1$ than visible light, X-rays, and radio waves that are subject to scatterings and attenuation.

In addition, the two-photon annihilation ($\gamma\gamma \to e^+e^-$) due to interactions with SN photons is crucial above a cutoff energy at ∼20–30 GeV, which is consistent with $E_\gamma (3k\mathcal{T}_{\rm sn}) \approx m_e^2 c^4$. Note that we have assumed a constant SN temperature of $\mathcal{T}_{\rm sn} = 9000$ K assuming the graybody radiation. Electrons and positrons from muon decay, as well as those from $\gamma\gamma \to e^+e^-$, radiatively cool mainly via synchrotron radiation, but a fraction of their energy is used for inverse Compton emission, which can be seen below ∼0.1 GeV energies. The light curves are shown in Figure 3, where one sees that the gamma-ray attenuation in the CSM can be important until ∼100 days, which makes the predictions for gamma-ray light curves different from those without the attenuation effects.

We consider light curves from $t = 20$ to 316 days. The time window of our theoretical calculation and *Fermi*-LAT gamma-ray search is motivated by the sharp decline of the observed optical light curve at $t \sim 300$ days. Its origin has been under debate (e.g., Maeda et al. 2013; Ofek et al. 2014b), and there may be a break in the bolometric light curve itself (Fransson et al. 2014). The gamma-ray and neutrino luminosities are proportional to $\min[1, f_{pp}]\epsilon_p L_s$. With $f_{pp} \gtrsim 1$, they will trace the bolometric luminosity that could abruptly drop after the shock reaches the edge of the CSM (whose radius is characterized by R_w).

We also calculate radio light curves in Figure 4. However, as expected, radio emission is strongly suppressed, due to strong absorption in the CSM, as well as synchrotron self-absorption in the radiation zone. In particular, the free–free absorption process is crucial, especially when the pre-shock CSM is uniform and spherical, and we do not expect radio detection even if we assume a rather high temperature of $\mathcal{T}^u_{\rm cs} = 3 \times 10^5$ K. However, a fraction of the radio emission could escape if the CSM is aspherical or even clumpy, which has been suggested observationally for some SNe IIn (Margutti et al. 2014a; Smith 2014). Also, a fraction of escaping radio waves could be enhanced if the pre-shock CSM is mostly neutral. To discuss this effect, we here assume that 3% of the emission can escape because of the possible incomplete CSM

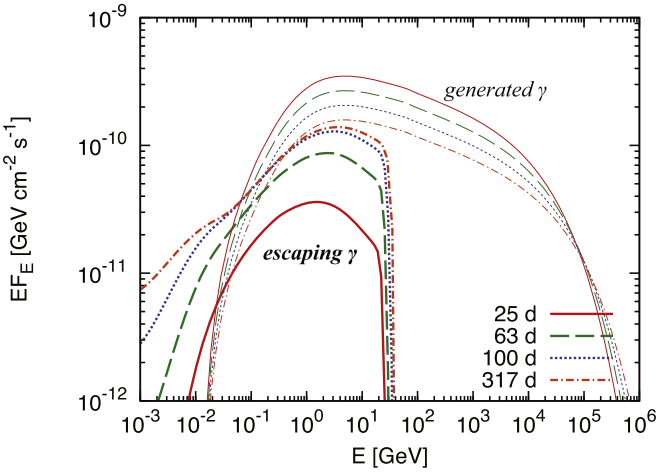

Figure 2. Theoretical predictions for hadronic gamma-ray spectra from SN 2010jl at different times, obtained by our time-dependent numerical model. We show cases after (thick curves) and before (thin curves) gamma-ray attenuation in the CSM. Note that electromagnetic cascades in the radiation zone are taken into account. The CR parameters are $\epsilon_p = 0.05$ and $s_p = 2.2$.

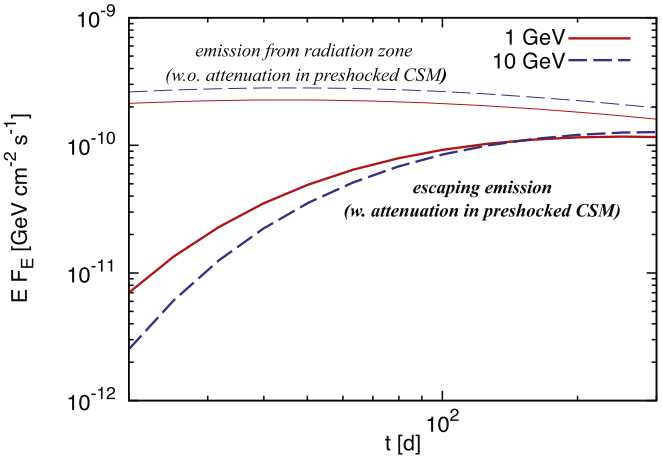

Figure 3. Modeled hadronic gamma-ray light curves of SN 2010jl, corresponding to Figures 1 and 2. Possible gamma-ray attenuation in the GeV range, indicated by the thick curves, is dominated by the Bethe–Heitler pair-production process in the pre-shock CSM. Note that this attenuation is irrelevant for late-time emission that dominates the gamma-ray fluence.

coverage, while the attenuation due to radiation fields is fully taken into account. The radio emission from SN 2010jl had not been detected for about a year, which is consistent with the strong absorption. The radio observations of SN 2010jl were carried out with the Karl G. Jansky Very Large Array, and detections were reported ∼600–700 days after the explosion (Chandra et al. 2015). Although the detailed modeling of the radio emission is beyond the scope of this work, the radio data show a late-time flux with ∼0.1 mJy, which is roughly consistent with our predictions of the hadronic scenario if ∼3% of the emission can avoid interactions with electrons in the matter.

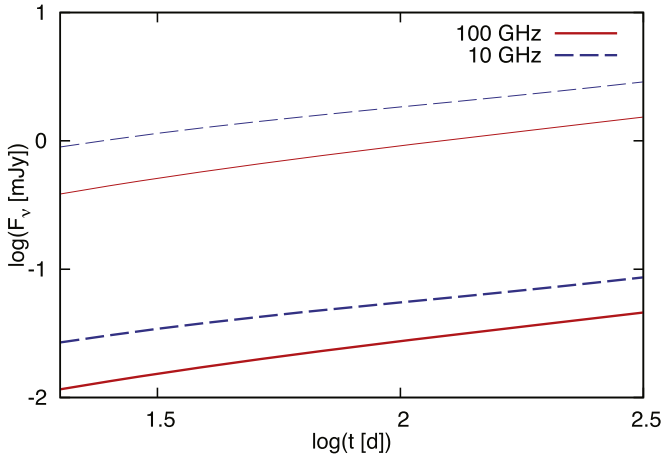

Figure 4. Radio light curves corresponding to Figure 3. The attenuation of radio waves during the CSM propagation is too strong. We here show cases for radio emission from the radiation zone (thin curves) and escaping emission for $f_{\rm esc}^{\rm mat} = 0.03$ (thick curves).

3.2. Fermi-*LAT Data Analysis and Implications*

Dedicated searches for gamma-ray emission from interaction SNe were first performed by Ackermann et al. (2015). The SN sample used in the past stacking analysis includes SN 2010jl. In this work, focusing on SN 2010jl, we reanalyze the *Fermi*-LAT data with the Pass 8 SOURCE class.[18] There are two significant improvements compared to the previous work. First, observationally, the Pass 8 data benefit from improved reconstruction and event selection algorithms with respect to the previous data release Pass 7, leading to a significantly improved angular resolution and sensitivity (Atwood et al. 2009), and therefore provide improved gamma-ray constraints. Second, the rich observational data on SN 2010jl allow us to derive detailed physical constraints on the possibility of CR ion acceleration in interacting SNe. In Ackermann et al. (2015), simple gamma-ray spectra with neither attenuation nor cascades were used, whereas we employ more realistic gamma-ray spectra by including these detailed effects. Also, thanks to the time-dependent multiwavelength data for the SN, we are able to convert the gamma-ray limits into the bounds on the CR energy fraction, which is the quantity of particular interest.

We perform a binned analysis (i.e., binned in space and energy) using the standard *Fermi*-LAT Science-Tools package version v10r01p01 available from the Fermi Science Support Center[19] (FSSC) and the P8R2_SOURCE_V6 instrument response functions. Otherwise, the analysis is identical to the one described in Ackermann et al. (2015). The results of our updated gamma-ray data analysis at different integration times are shown in Figure 5. We here plot the logarithm of the likelihood ratio, $-\Delta \ln \mathcal{L} \equiv \ln(\mathcal{L}/\mathcal{L}_0)$, as a function of energy. Here $\mathcal{L}_0$ is the likelihood evaluated at the best-fit parameters under a background-only hypothesis, whereas $\mathcal{L}$ is the likelihood evaluated at the best-fit model parameters with a candidate point source at the SN position. See Ackermann et al. (2015) for details on the likelihood analysis.

Both differential and spectrum-integrated upper limits on gamma-ray fluxes averaged over a given time window are shown. At lower energies, the flux sensitivity approximately scales as $\propto t^{-1/2}$, as expected in the background-dominated regime. At high energies, it scales as $\propto t^{-1}$ at early times and then becomes $\propto t^{-1/2}$. Note that the spectrum-integrated flux limits that depend on theoretical flux templates are typically several times stronger than the differential flux limits, for a hard spectrum with $s \sim 2$.

Based on these results, we place quantitative limits on the energy fraction of CR protons, ϵ_p. This is done by convolving the gamma-ray spectra obtained by the theoretical calculations (Section 3) and the differential upper limits shown in Figures 5 and 6. For different integration times from 20 to 50.24 days, 20 to 100.24 days, and 20 to 251.79 days, the derived 95% CL limits for $s_p = 2.2$ are $\epsilon_p \leqslant 0.75\,(\epsilon_{\rm sn}/0.25)$, $\epsilon_p \leqslant 0.21\,(\epsilon_{\rm sn}/0.25)$, and $\epsilon_p \leqslant 0.066\,(\epsilon_{\rm sn}/0.25)$, respectively. See Figure 1 for the comparison between our theoretical predictions and the gamma-ray limit from the *Fermi*-LAT data. In Figure 1, the possible effect of gamma-ray attenuation in the pre-shock CSM is also indicated, and the constraints on ϵ_p can be somewhat improved if the gamma-ray attenuation in the CSM is completely negligible. Note that $\epsilon_p = 0.05$, which is indicated by the observation of the Galactic SNR Cas A, is still consistent with the nondetection of gamma-rays from this SN IIn, and the upper limit can be somewhat weaker for larger values of $\epsilon_{\rm sn}$ (as we are constraining $\epsilon_p L_s = (\epsilon_p/\epsilon_{\rm sn}) L_{\rm sn}$ via Equation (19)). Nevertheless, our result, say, $\epsilon_p \lesssim 0.1$ more conservatively, clearly suggests that we have reached the interesting parameter space for the purpose of probing the CR ion acceleration in embryonic SNRs embedded in a high-density material.

The constraints on ϵ_p are quite insensitive to s_p, because the predicted GeV gamma-ray spectra are similar for different values of s_p (see Figure 7 below). Based on the results shown in Figure 6 from left to right, we obtain $\epsilon_p \leqslant 0.047\,(\epsilon_{\rm sn}/0.25)$ (for $s_p = 2.0$), $\epsilon_p \leqslant 0.052\,(\epsilon_{\rm sn}/0.25)$ (for $s_p = 2.2$), and $\epsilon_p \leqslant 0.073\,(\epsilon_{\rm sn}/0.25)$ (for $s_p = 2.4$), respectively. In any case, given that there are uncertainties in the source parameters used in our theoretical model, we conclude that the CR ion energy fraction in SN 2010jl is constrained to be less than $\sim$10%. Note that Figure 1 corresponds to the case for $s_p = 2.2$.

4. Simplified Model

In the previous sections, we described the time-dependent model to calculate nonthermal emissions from interacting SNe and considered SN 2010jl as one of the applications. As shown in Murase (2018), such a time-dependent model is essential, because the detectability of high-energy neutrinos and gamma-rays depends on the signal-to-background ratio for such *long-duration transients*. However, detailed SN data in the optical band and/or at other wavelengths may not always be available. Then, a simpler model can still be useful in such cases where the quality of the observational data is rather limited. In the following, we consider a simplified version of the model (which is essentially a single-zone nonthermal radiation model with external thermal radiation fields), for a given set of the principal parameters (n_N, R_s, and V_s) that represent typical values during the time interval of interest and may be obtained observationally for a specific characteristic period. The setup is similar to that in Murase et al. (2011), but we present more detailed calculations on electromagnetic cascades, as well as attenuation during the photon propagation in the pre-shock CSM.

[18] http://fermi.gsfc.nasa.gov/ssc/data/analysis/documentation/Pass8_usage.html
[19] http://fermi.gsfc.nasa.gov/ssc/data/analysis/

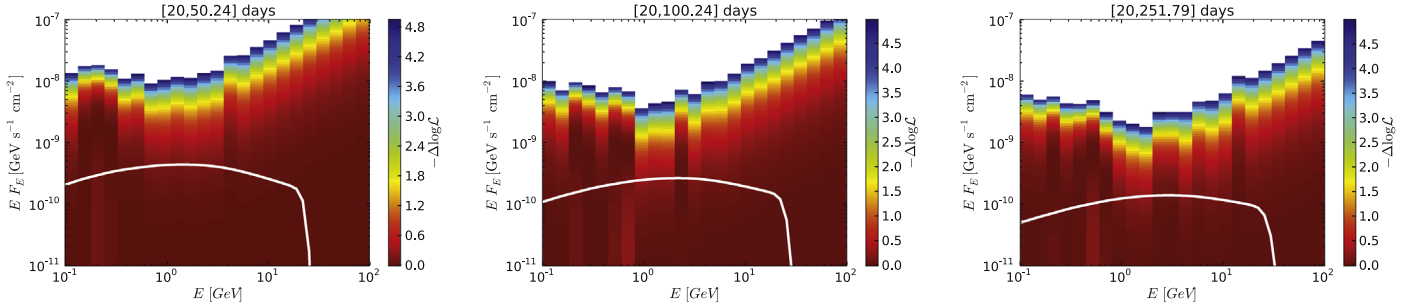

Figure 5. *Fermi*-LAT constraints on gamma-ray fluxes from SN 2010jl, for different integration times from 20 to 50.24 days (left), 20 to 100.24 days (middle), and 20 to 251.79 days (right). Within each energy bin, the color scale denotes the variation of the logarithm of the likelihood with respect to the best-fit value of the SN flux for a given time window. We test a putative source at the SN position and construct the bin-by-bin likelihood function. Then, the bin-by-bin likelihood is calculated by scanning the integrated energy flux of the SN within each energy bin. The theoretical expected fluxes for $s_p = 2.2$, averaged over time windows, are shown as solid curves (with gamma-ray attenuation in the pre-shock CSM).

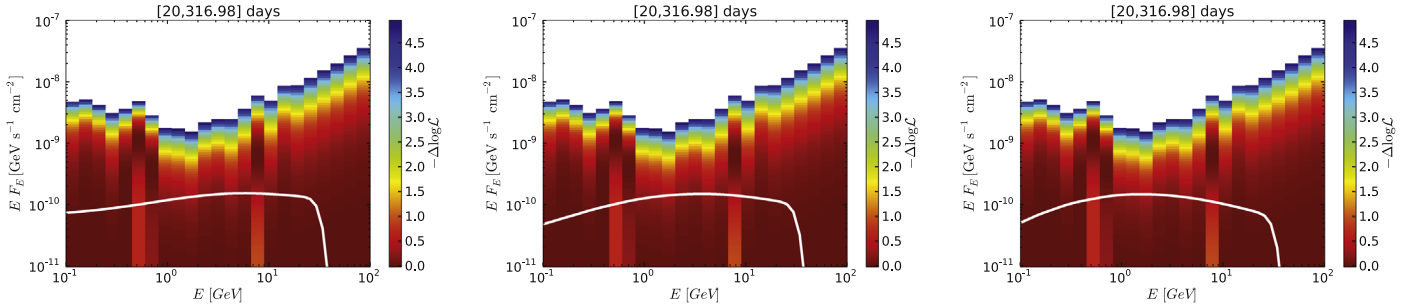

Figure 6. *Fermi*-LAT constraints on gamma-ray fluxes from SN 2010jl for an integration time from 20 to 316.98 days. Similar to Figure 5, but the CR spectral index is set to 2.0 (left), 2.2 (middle), and 2.4 (right), respectively.

First, we apply the simplified model to SN 2010jl as an example. The model parameters are listed in Table 2, which are based on the observations at $t \sim 300$ days (Fransson et al. 2014; Ofek et al. 2014b). The neutrino and gamma-ray spectra are shown in Figure 7. One clearly sees the dependence of neutrino and gamma-ray fluences on s_p from this panel. Very importantly, results on GeV gamma-ray fluences are insensitive to s_p. With the same ϵ_p, GeV neutrino and gamma-ray fluences are higher for larger values of s_p, but electromagnetic cascades are more important for harder indices, which compensates the fluence difference. The component of CR-induced cascades is clearly evident below the kinematic break of π^0 decay at $E_\gamma \approx m_{\pi^0} c^2/2 \simeq 67.5$ MeV. The results agree with those of the time-dependent model (compare Figure 7 to 1). This implies that the simplified model is valid enough for the purpose of understanding physical properties of the emission. However, in general, this depends on parameters, and the time-dependent model is always better given that sufficient data are available.

In Figure 8, we also show broadband nonthermal spectra for both hadronic and leptonic components. Pionic gamma-rays produced via $\pi^0 \to \gamma\gamma$ are denoted by "generated γ." The spectra from the radiation zone are also depicted by the upper curves of the shaded regions, where the attenuation in the pre-shock CSM (i.e., the shock upstream) is not included yet. We find that low-frequency radio emission is modified compared to simple predictions of synchrotron emission from relativistic electrons with a simple power-law injection spectrum. This is because the Coulomb cooling of electrons and positrons becomes relevant in high-density environments, making the spectrum harder by distorting the lepton distribution and suppressing the resulting synchrotron emission. In addition, we expect nonthermal X-ray emission because relativistic electrons and positrons up-scatter SN photons to an energy of $\sim \gamma_h^2 3kT_{\rm sn} \sim 12\,{\rm keV}\,\mathcal{T}_{\rm sn,4}$, where $\gamma_h \approx 68$. In reality, we expect strong photoelectric absorption and subsequent thermalization in the pre-shock CSM, so soft X-rays are significantly suppressed in the SN 2010jl-like cases. Also, the nonthermal X-ray component can readily be overwhelmed by the thermal bremsstrahlung component. We also consider the leptonic scenario, in which the emission would be weaker for $\epsilon_e/\epsilon_p \sim 10^{-3}$ to 10^{-2}. The radio emission is significantly suppressed by the synchrotron self-absorption, as well as the free–free absorption in the pre-shock CSM. Note that our model predicts the existence of *both* hadronic and leptonic components. However, for SNe IIn like SN 2010jl, the hadronic component is expected to be dominant over the entire energy range. Thus, the model prediction consisting of the sum of the two components is essentially the same as that of the hadronic scenario. The predicted radio flux is consistent with upper limits at ∼200–300 days, provided by Chandra et al. (2015) and Chandra (2018). See Figure 8, where the upper limit at 22.5 GHz, measured at 204 days after the explosion, is shown. Note that it also supports that the radio signals should be absorbed in the CSM. The model fluxes are even more strongly suppressed at lower frequencies, and the radio data at 22.5 GHz give the most relevant constraint on the model.

Second, we apply our code to SN 2014C, which occurred at $d = 15.1$ Mpc. This SN was initially classified as an SN Ib, but in a year it started showing strong interactions with a dense CSM with $M_{\rm cs} \sim 1.0$–$1.5\,M_\odot$. The model parameters listed in Table 3 are taken from the observational data at $t \sim 400$ days

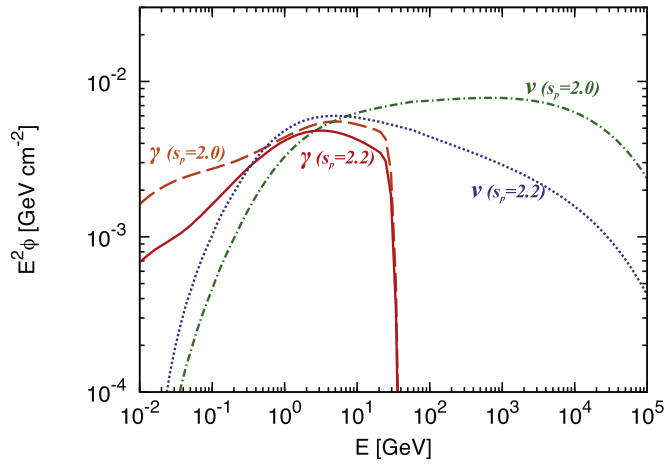

Figure 7. Gamma-ray and (all-flavor) neutrino spectra expected for SN 2010jl. This panel shows results for different CR spectral indices, and GeV gamma-ray fluences are insensitive to s_p. The simplified model is used. Both electromagnetic cascades in the radiation zone and attenuation in the pre-shock CSM are taken into account. The energy fraction carried by CRs is $\epsilon_p = 0.05$.

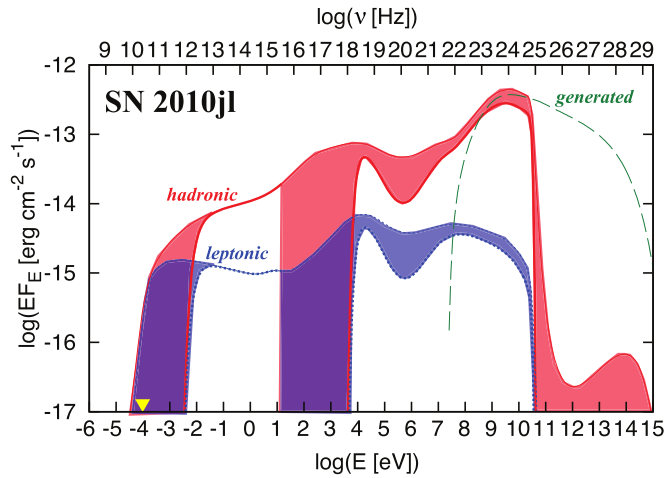

Figure 8. Broadband nonthermal spectra from SN IIn 2010jl at $t = 300$ days. The simplified model is used. The upper curves of the shaded regions indicate fluxes from the radiation zone, whereas the lower curves correspond to the cases where attenuation in the pre-shock CSM is implemented. The CR parameters are $\epsilon_p = 0.05$ and $s_p = 2.2$. The source distance is $d = 49$ Mpc. The radio upper limit (indicated by the triangle) is taken from Chandra et al. (2015) and Chandra (2018).

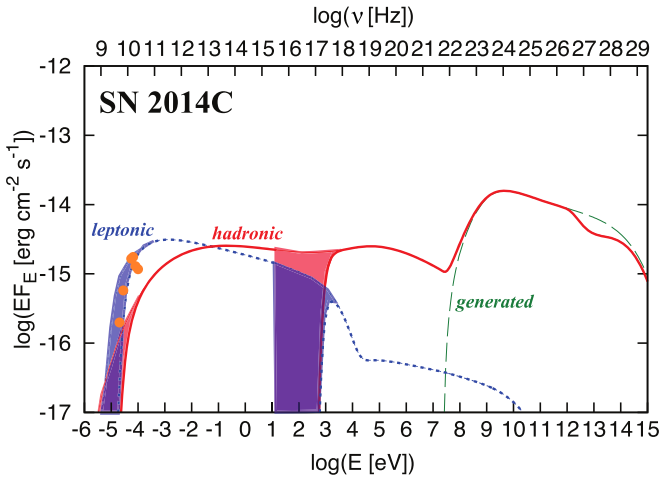

Figure 9. Broadband nonthermal spectra from strongly interacting Type Ib SN 2014C at $t = 396$ days. The simplified model is used. The CR parameters are $\epsilon_p = 0.05$ and $s_p = 2.2$. The source distance is $d = 15.1$ Mpc. Radio data (indicated by the filled circles) are taken from Margutti et al. (2017).

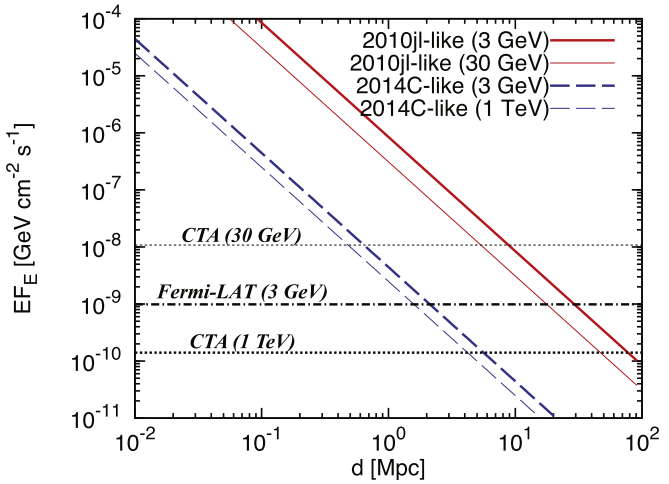

Figure 10. Discovery horizon of hadronic gamma-rays from interacting SNe with $\epsilon_p = 0.1$. For theory lines, the simplified model is considered for both SN 2010jl-like and SN 2014C-like emissions. Differential sensitivities of *Fermi*-LAT (for an observation time of 1 yr based on the survey-mode Pass 8 sensitivity at the north Galactic pole) and CTA (for an observation time of 50 hr) are used (Actis et al. 2011).

(Milisavljevic et al. 2015; Margutti et al. 2017). In this case, the observations indicated that the CSM has a "shell-like" structure, so we consider $\Delta R_s < R_s$, and the CSM mass should be written as $M_{\rm cs} \approx \Delta\Omega R_s^2 \Delta R_s m_H n_N$. The forward shock is nonradiative. X-ray emission, which is consistent with bremsstrahlung emission, was observed by *Chandra* and *NuSTAR* (Margutti et al. 2017). We here implement the X-ray luminosity, $L_X = 5 \times 10^{40}\,{\rm erg\,s^{-1}}$, and the X-ray temperature, $k\mathcal{T}_X = 18$ keV, inferred from these observations. In any case, the results on photon spectra are not affected by target photons in the X-ray range. Thermal emission in the optical band already declined at such late times, and the long-lasting dust emission was observed in the infrared band. For simplicity, we use $L_{\rm sn} = 7 \times 10^{40}\,{\rm erg\,s^{-1}}$ and $\mathcal{T}_{\rm sn} = 600$ K following Tinyanont et al. (2016). The resulting spectra are shown in Figure 9. In this case, the gamma-ray emission would be too dim to detect because the CSM density is not high enough for the CR calorimetry to hold. The pionic gamma-ray component can be attenuated by the infrared photons only modestly in the 10 TeV range. Because of an electromagnetic cascade and the inverse Compton scattering of the dust photons, the hadronic photon spectrum is flatter than the leptonic one. See also Model B in Murase et al. (2011). The radio signal in the 1–10 GHz range was detected (Margutti et al. 2017), which seems best explained by synchrotron emission from primary electrons (i.e., the leptonic interpretation). Note that the dominance of the leptonic component at sufficiently low frequencies is one of our predictions, as long as the CSM density is so large that the suppression is too strong (see also Murase et al. 2013). The Lorentz factor of secondary electrons and positrons is fixed at $\sim m_\pi/(4m_e)$, so the hadronic component has a corresponding low-energy break, as discussed in Section 2. Then the leptonic component eventually

Table 2
Source Parameters of SN 2010jl, Which Are Used in the Simplified Model

Name	n_N (cm)	R_s (cm)	V_s (cm s^{-1})	$L_{\rm sn}$ (erg s^{-1})	$\mathcal{T}_{\rm sn}$ (K)	ϵ_B	ϵ_p	ϵ_e
SN 2010jl	1.8×10^9	1×10^{16}	4×10^8	2.7×10^{43}	9000	1.5×10^{-2}	0.05	5×10^{-4}

Note. The CSM size is assumed to be $\Delta R_s \approx R_s$. The derived shock power corresponds to $\epsilon_{\rm sn} = 0.25$.

Table 3
Source Parameters of SN 2014C, Which Are Used in the Simplified Model

Name	n_N (cm)	R_s (cm)	V_s (cm s^{-1})	$L_{\rm sn}$ (erg s^{-1})	$\mathcal{T}_{\rm sn}$ (K)	ϵ_B	ϵ_p	ϵ_e
SN 2014C	3.5×10^6	6.4×10^{16}	4×10^8	7×10^{40}	600	1.5×10^{-2}	0.05	2×10^{-4}

Note. Motivated by observations (Margutti et al. 2017), we assume a CSM shell with $\Delta R_s = 1.0 \times 10^{16}$ cm.

takes over at low frequencies, as one can see in Figure 9. Although we show the case of $\mathcal{T}^u_{\rm cs} = 3 \times 10^5$ K for demonstration, the free–free absorption can be more significant for a lower temperature of $\mathcal{T}^u_{\rm cs} \sim 10^4$–$10^5$ K. More detailed modeling that takes into account the CSM geometry would be necessary to robustly constrain ϵ_p and ϵ_e. In any case, the model (with a CR ion energy fraction of $\epsilon_p \sim 0.01$–0.1) predicts a hard spectrum of radio emission from secondary electrons and positrons, with a detectable flux of $F_\nu \sim 1$ mJy at ∼100–300 GHz. Thus, *higher-frequency* observations are essential to critically test the existence of the hadronic component.

5. Gamma-Ray Detectability of Nearby Interacting Supernovae

Can we detect high-energy gamma-ray emission from nearby extragalactic SNe? For ordinary SNe II, the *Fermi*-LAT detection is possible up to a few megaparsecs (Murase 2018), for CSM environments suggested by SN 2013fs. SNe IIn with a much higher CSM density, which this work focuses on, are more promising targets for the purpose of detecting extragalactic SNe. In order to address this question, using SN 2010jl and SN 2014C as gamma-ray spectrum templates (see Section 4), we compare the theoretical fluxes to differential sensitivities of *Fermi*-LAT and the Cerenkov Telescope Array (CTA). See Figure 10. For the SN 2010jl-like cases, GeV gamma-ray signal can be seen by *Fermi* up to ∼30–50 Mpc, whereas detections with IACTs may be more difficult, especially in the TeV range because of the severe gamma-ray attenuation due to the two-photon annihilation process. These features are qualitatively consistent with the previous findings by Murase et al. (2011). Note that we have used differential sensitivities, which give conservative estimates on the detectability. Indeed, the discovery horizons indicated in Figure 10 are somewhat worse than ∼50 Mpc suggested from the dedicated analysis presented in Section 3. For the SN 2014C-like cases, TeV gamma-ray attenuation in the pre-shock CSM is irrelevant. Therefore, observations with ground Cerenkov telescopes will be more powerful, and CTA can detect the interacting SNe up to ∼5–8 Mpc. The rate of Type IIn is ∼7%–9% of all the core-collapse SNe (e.g., Li et al. 2011; Smith et al. 2011), and the occurrence rate of nearby SNe IIn within 30 Mpc is ∼1 yr^{-1}. The rate of SNe IIn within 10 Mpc is thus ∼0.03 yr^{-1}, but this value is conservative because the SN rate density within 10 Mpc is higher than the global one (Horiuchi et al. 2011). Because high-energy neutrinos from Type IIn are detectable by IceCube up to ∼10 Mpc (Murase et al. 2011; Petropoulou et al. 2017), interacting SNe should be regarded as promising sources for multimessenger observations.

6. Summary

Our results are summarized as follows:

(a) We numerically calculated broadband spectra of CR-induced nonthermal emission from interacting SNe, taking into account various processes such as electromagnetic cascades in the post-shock CSM and the attenuation in the pre-shock CSM. The electromagnetic cascade is unavoidable, although its detailed effect was not included in the previous literature (Murase et al. 2011; Petropoulou et al. 2016; Zirakashvili & Ptuskin 2016). We found that GeV gamma-ray spectra are insensitive to s_p thanks to the cascade, and the attenuation effect can reduce the flux only modestly, which ensures that gamma-rays can be used as a probe of shock interactions in dense environments that are difficult to directly observe in visible light, X-rays, and radio waves. The phenomenological prescription we presented in this work enables us to robustly predict high-energy nonthermal signatures only with a few free parameters, given that the SN dynamics is determined by optical and X-ray observations. In the early stages of interactions, the deceleration of a fast velocity component of the SN ejecta dominates the dissipation. This enhances gamma-ray and neutrino fluxes by about one order of magnitude (Murase 2018), which can be taken into account in our formalism.

(b) We applied our phenomenological time-dependent model to SN IIn 2010jl, by which for the first time we derived the gamma-ray constraint on the CR energy fraction. This cannot be done without the detailed modeling of high-energy emission. In addition, we reanalyzed the *Fermi*-LAT data, taking advantage of the new Pass 8 data release, and updated the gamma-ray limits themselves. With both theoretical and observational improvements, we obtained the new constraint on the CR energy fraction, $\epsilon_p \lesssim 0.05$–0.1. Within uncertainties, our results are consistent with the DSA theory of CRs, as well as the observations of Galactic SNRs such as Cas A, but can be regarded as intriguing constraints on the CR ion acceleration in early SNe in dense environments.

(c) We considered both hadronic and leptonic components with the simplified model and discussed the detectability

of gamma-ray emission from nearby interacting SNe. High-energy gamma-ray and neutrino signals from SNe IIn may be observed in the near future.

(d) High-frequency radio emission from secondary electrons and positrons is a promising signature of CR ion acceleration in interacting SNe, although the CSM geometry is important for the detectability. Although detailed modeling is left for future work, our model predictions are consistent with the available radio data of Type IIn SN 2010jl and strongly interacting Type Ib SN 2014C.

If the DSA theory is correct, it is natural to expect efficient acceleration of CR ions even in early stages of SNe. Particle acceleration at high-density environments has been suggested by observations of gamma-rays from novae (Ackermann et al. 2014). While the SNe and novae could still share some features, the nova shock is usually slower, and other physical conditions may differ from the SN case, so both observations are relevant as independent information. For novae, the recent concurrent observation of optical and gamma-ray emission indicates $\epsilon_p \sim 1\%$ assuming that the optical emission is powered by the shock (Li et al. 2017). Although the gamma-ray attenuation is more important at lower-velocity shocks in general (Murase et al. 2014), such a low efficiency could be an outcome of the magnetic field perpendicular to the shock normal. However, for interacting SNe, the magnetic field geometry is highly uncertain. The shock is more powerful, and CSM eruptions would be transient, also involving shocks and turbulences. Thus, constraints or detections will help us understand the physics of the DSA, as well as pre-SN mass-loss mechanisms. In addition, these are important to address the origin of CRs around or beyond the knee energy and figure out their contribution to the diffuse neutrino flux observed in IceCube (Sveshnikova 2003; Murase et al. 2014; Zirakashvili & Ptuskin 2016; Petropoulou et al. 2017). Astrophysical sources producing neutrinos via inelastic *pp* collisions, if they significantly contribute to the diffuse neutrino flux, cannot avoid constraints from the isotropic diffuse gamma-ray background in the GeV–TeV range (Murase et al. 2013). Our results indicate that SNe IIn like SN 2010jl can serve as hidden CR accelerators (Murase et al. 2016) just after the photon breakout, so they can alleviate the gamma-ray limits even though only a moderate fraction of the GeV gamma-rays can be attenuated. On the other hand, SNe like SN 2014C do not suffer from the gamma-ray attenuation, so the diffuse gamma-ray background constraints can be important. High-energy emission from ordinary SNe such as Type II-P, II-L, and IIb SNe has also been predicted to be detectable for nearby SNe (Murase 2018), and our method is applicable to these objects. Future multi-messenger observations will give us important clues to this long-standing enigma of particle astrophysics.

Kohta Murase thanks Poonam Chandra, Boaz Katz, Eran Ofek, Todd Thompson, and Eli Waxman for useful discussions. We also thank internal referees in the *Fermi*-LAT Collaboration, especially Regina Caputo, Seth Digel, Nicola Omodei, and Nicolas Renault-Tinacci for reviewing the manuscript. The work of Kohta Murase is supported by NSF grant No. PHY-1620777 and the Alfred P. Sloan Foundation. He also acknowledges the Hubble Fellowship through NASA and STScI during the early stages of this work. A.F. was supported by the Initiative and Networking Fund of the Helmholtz Association. Keiichi Maeda acknowledges support by JSPS KAKENHI grant Nos. 18H04585, 18H05223, 17H02864. J.F.B. is supported by NSF grant No. PHY-1714479. The preliminary estimates and results were presented at the PCTS workshop at Princeton University in 2015, the AMON workshop at Penn State University in 2015, and the supernova workshop at ISSI in 2016.

The *Fermi*-LAT Collaboration acknowledges generous ongoing support from a number of agencies and institutes that have supported both the development and the operation of the LAT, as well as scientific data analysis. These include the National Aeronautics and Space Administration and the Department of Energy in the United States; the Commissariat à l'Energie Atomique and the Centre National de la Recherche Scientifique Institut National de Physique Nucléaire et de Physique des Particules in France; the Agenzia Spaziale Italiana and the Istituto Nazionale di Fisica Nucleare in Italy; the Ministry of Education, Culture, Sports, Science and Technology (MEXT), High Energy Accelerator Research Organization (KEK), and Japan Aerospace Exploration Agency (JAXA) in Japan; and the K. A. Wallenberg Foundation, the Swedish Research Council, and the Swedish National Space Board in Sweden. Additional support for science analysis during the operations phase is gratefully acknowledged from the Istituto Nazionale di Astrofisica in Italy and the Centre National d'Études Spatiales in France. This work was performed in part under DOE Contract DE-AC02-76SF00515.

ORCID iDs

Kohta Murase https://orcid.org/0000-0002-5358-5642
Anna Franckowiak https://orcid.org/0000-0002-5605-2219
Raffaella Margutti https://orcid.org/0000-0003-4768-7586
John F. Beacom https://orcid.org/0000-0002-0005-2631

References

Ackermann, M., Ajello, M., Albert, A., et al. 2014, Sci, 345, 554
Ackermann, M., Arcavi, I., Baldini, L., et al. 2015, ApJ, 807, 169
Actis, M., Agnetta, G., Aharonian, F., et al. 2011, ExA, 32, 193
Ahnen, M. L., Ansoldi, S., Antonelli, L. A., et al. 2018, MNRAS, 476, 2874
Atwood, W. B., Abdo, A. A., Ackermann, M., et al. 2009, ApJ, 697, 1071
Caprioli, D. 2016, in 34th International Cosmic Ray Conf. (ICRC2015), Vol. 236, Cosmic-ray acceleration and propagation (Trieste: PoS), 008, doi:10.22323/1.236.0008)
Caprioli, D., & Spitkovsky, A. 2014a, ApJ, 783, 91
Caprioli, D., & Spitkovsky, A. 2014b, ApJ, 794, 46
Chandra, P. 2018, SScRv, 214, 27
Chandra, P., Chevalier, R. A., Chugai, N., Fransson, C., & Soderberg, A. M. 2015, ApJ, 810, 32
Chevalier, R. A. 1982, ApJ, 258, 790
Chevalier, R. A., & Fransson, C. 2017, Handbook of Supernovae (Cham: Springer International)
Chevalier, R. A., Fransson, C., & Nymark, T. K. 2006, ApJ, 641, 1029
Chodorowski, M. J., Zdziarski, A. A., & Sikora, M. 1992, ApJ, 400, 181
Drury, L. O. 1983, RPPh, 46, 973
Fransson, C., Ergon, M., Challis, P. J., et al. 2014, ApJ, 797, 118
Funk, S. 2015, ARNPS, 65, 245
Horiuchi, S., Beacom, J. F., Kochanek, C. S., et al. 2011, ApJ, 738, 154
Immler, S., Modjaz, M., Landsman, W., et al. 2008, ApJL, 674, L85
Jackson, J. D. 1975, Classical Electrodynamics (New York: Wiley)
Kafexhiu, E., Aharonian, F., Taylor, A. M., & Vila, G. S. 2014, PhRvD, 90, 123014
Katsuda, S., Maeda, K., Bamba, A., et al. 2016, ApJ, 832, 194
Katz, B., Sapir, N., & Waxman, E. 2012, in IAU Symp. 279, Death of Massive Stars: Supernovae and Gamma-Ray Bursts (Cambridge: Cambridge Univ. Press), 274
Katz, B., & Waxman, E. 2008, JCAP, 0801, 018

Kelner, S. R., Aharonian, F. A., & Bugayov, V. V. 2006, PhRvD, 74, 034018
Li, K.-L., et al. 2017, NatAs, 1, 0222
Li, W., Leaman, J., Chornock, R., et al. 2011, MNRAS, 412, 1441
Maeda, K. 2012, ApJ, 758, 81
Maeda, K. 2013, ApJ, 762, 14
Maeda, K., et al. 2013, ApJ, 776, 5
Margutti, R., Kamble, A., Milisavljevic, D., et al. 2017, ApJ, 835, 140
Margutti, R., Milisavljevic, D., Soderberg, A. M., et al. 2014a, ApJ, 780, 21
Margutti, R., Milisavljevic, D., Soderberg, A. M., et al. 2014b, ApJ, 797, 107
Matsumoto, Y., Amano, T., Kato, T. N., & Hoshino, M. 2017, PhRvL, 119, 105101
Matzner, C. D., & McKee, C. F. 1999, ApJ, 510, 379
Mauerhan, J., Williams, G. G., Smith, N., et al. 2014, MNRAS, 442, 1166
Mészáros, P. 2006, RPPh, 69, 2259
Milisavljevic, D., Margutti, R., Kamble, A., et al. 2015, ApJ, 815, 120
Miller, A. A., Chornock, R., Perley, D. A., et al. 2009, ApJ, 690, 1303
Moriya, T. J., Maeda, K., Taddia, F., et al. 2013, MNRAS, 435, 1520
Morrison, R., & McCammon, D. 1983, ApJ, 270, 119
Murase, K. 2008, PhRvD, 78, 101302
Murase, K. 2018, PhRvD, 97, 081301
Murase, K., Ahlers, M., & Lacki, B. C. 2013, PhRvD, 88, 121301
Murase, K., Guetta, D., & Ahlers, M. 2016, PhRvL, 116, 071101
Murase, K., Kashiyama, K., Kiuchi, K., & Bartos, I. 2015, ApJ, 805, 82
Murase, K., Thompson, T. A., Lacki, B. C., & Beacom, J. F. 2011, PhRvD, 84, 043003
Murase, K., Thompson, T. A., & Ofek, E. O. 2014, MNRAS, 440, 2528
Nadezhin, D. K. 1985, Ap&SS, 112, 225
Ofek, E. O., Arcavi, I., Tal, D., et al. 2014a, ApJ, 788, 154
Ofek, E. O., Lin, L., Kouveliotou, C., et al. 2013a, ApJ, 768, 47
Ofek, E. O., Sullivan, M., Cenko, S. B., et al. 2013b, Natur, 494, 65
Ofek, E. O., Zoglauer, A., Boggs, S. E., et al. 2014b, ApJ, 781, 42
Ohira, Y., Murase, K., & Yamazaki, R. 2010, A&A, 513, A17
Park, J., Caprioli, D., & Spitkovsky, A. 2015, PhRvL, 114, 085003
Petropoulou, M., Coenders, S., Vasilopoulos, G., Kamble, A., & Sironi, L. 2017, MNRAS, 470, 1881
Petropoulou, M., Kamble, A., & Sironi, L. 2016, MNRAS, 460, 44
Rybicki, G. B., & Lightman, A. P. 1979, Radiative Processes in Astrophysics (New York: Wiley)
Schlickeiser, R. 2002, Cosmic Ray Astrophysics (Berlin: Springer)
Smith, N. 2013, MNRAS, 429, 2366
Smith, N. 2014, ARA&A, 52, 487
Smith, N., Li, W., Filippenko, A. V., & Chornock, R. 2011, MNRAS, 412, 1522
Smith, N., Li, W., Foley, R. J., et al. 2009, ApJ, 695, 1334
Smith, N., & McCray, R. 2007, ApJL, 671, L17
Smith, N., Silverman, J. M., Chornock, R., et al. 2007, ApJ, 666, 1116
Sveshnikova, L. G. 2003, A&A, 409, 799
Tinyanont, S., Kasliwal, M. M., Fox, O. D., et al. 2016, ApJ, 833, 231
van Marle, A. J., Smith, N., Owocki, S. P., & van Veelen, B. 2010, MNRAS, 407, 2305
Weaver, T. A. 1976, ApJS, 32, 233
Xu, S., & Lazarian, A. 2017, ApJ, 850, 126
Yamazaki, R., Kohri, K., Bamba, A., et al. 2006, MNRAS, 371, 1975
Zirakashvili, V. N., & Ptuskin, V. S. 2016, APh, 78, 28